

# Nanoscale

Accepted Manuscript



This is an *Accepted Manuscript*, which has been through the Royal Society of Chemistry peer review process and has been accepted for publication.

*Accepted Manuscripts* are published online shortly after acceptance, before technical editing, formatting and proof reading. Using this free service, authors can make their results available to the community, in citable form, before we publish the edited article. We will replace this *Accepted Manuscript* with the edited and formatted *Advance Article* as soon as it is available.

You can find more information about *Accepted Manuscripts* in the [Information for Authors](#).

Please note that technical editing may introduce minor changes to the text and/or graphics, which may alter content. The journal's standard [Terms & Conditions](#) and the [Ethical guidelines](#) still apply. In no event shall the Royal Society of Chemistry be held responsible for any errors or omissions in this *Accepted Manuscript* or any consequences arising from the use of any information it contains.

# Realization of High Curie Temperature Ferromagnetism in Atomically Thin MoS<sub>2</sub>, WS<sub>2</sub> Nanosheets with Uniform and Flower-like Morphology

Zhaolong Yang,<sup>†</sup> Daqiang Gao,<sup>†\*</sup> Jing Zhang,<sup>‡</sup> Qiang Xu,<sup>†</sup> Shoupeng Shi,<sup>†</sup> Kun Tao<sup>†</sup> and Desheng Xue<sup>†\*</sup>

Received Xth XXXXXXXXXXXX 20XX, Accepted Xth XXXXXXXXXXXX 20XX

First published on the web Xth XXXXXXXXXXXX 200X

DOI: 10.1039/b000000x

High Curie temperature ferromagnetism has been realized in atomically thin MoS<sub>2</sub> and WS<sub>2</sub> nanosheets. The ultrathin nanosheet samples are prepared via a novel, simple and efficient chemical vapor deposition method; different kinds of transition metal disulfides (MoS<sub>2</sub> and WS<sub>2</sub>) could be obtained by sulphuring corresponding cation sources (MoO<sub>3</sub> and WCl<sub>6</sub>). Through related morphology and structure characterizations, we confirm that large-area, uniform, few-layer MoS<sub>2</sub> and WS<sub>2</sub> nanosheets were successfully synthesized by this method. Both nanosheet samples exhibit distinct ferromagnetic behavior. By careful measuring and fitting of the magnetization of MoS<sub>2</sub> and WS<sub>2</sub> samples at different temperatures, we decompose the magnetization into diamagnetic, paramagnetic and ferromagnetic contributions. The ferromagnetic contributions persist until 865 K for MoS<sub>2</sub> and 820 K for WS<sub>2</sub>. We attribute the observed ferromagnetic properties to the defects and dislocations produced during the growth process, as well as the presence of edge spins at the edge of the nanosheets.

## 1 Introduction

Atomically thin transition metal disulfides (TMDs), such as MoS<sub>2</sub> and WS<sub>2</sub>, have attract considerable attention owing to their unusual optical and electrical properties compared to their bulk forms.<sup>1–9</sup> As a kind of inorganic two-dimensional semiconductors with a direct bandgap, unlike zero-gap graphene and insulating hexagonal BN (*h*-BN), few-layer TMDs are promising candidates in fabricating nanodevices like field-effect transistors (FETs), photodetectors and gas sensors.<sup>1,2,5,7,10–14</sup> The FET based on the mechanically exfoliated monolayer MoS<sub>2</sub> nanosheet exhibits a high field-effect mobility ( $\sim 200 \text{ cm}^{-2} \text{ V}^{-1} \text{ s}^{-1}$ ) and current on/off ratio (exceeding  $1 \times 10^8$ ) with ultralow standby power.<sup>1</sup> Afterwards, monolayer MoS<sub>2</sub> photodetector was fabricated by Lopez-Sanchez et al., and it reaches very high photoresponsivity of  $880 \text{ AW}^{-1}$  due to the direct bandgap of monolayer MoS<sub>2</sub>.<sup>5</sup> Recently, Georgiou et al. demonstrated that WS<sub>2</sub> is a material as an ideal vertical barrier in the heterostructure FET which could significantly increase the current on/off ratio in a graphene-based transistor device.<sup>8</sup> Moreover, few-layer TMD materials, such as WS<sub>2</sub>, GaS and Mo-doped ReSe<sub>2</sub>, based

gas sensing photodetectors not only exhibit high-performance photoresponsivity but can response to both oxidizing gas and reducing gas, which was ascribed to the charge transfer between the sample surface and adsorbed gas molecules.<sup>14–16</sup> In addition, other potential applications of those layered-structure TMDs, such as nanotribology, moisture responsiveness, biomedicine, catalysis, lithium batteries and hydrogen storage have also been proposed and investigated.<sup>17–23</sup>

As complementary research to graphene, this area is still open to researchers because of its rich physics. Achieving ferromagnetic (FM) ordering in two-dimensional TMD materials provides another promising application in spintronic nanodevices.<sup>24–27</sup> Disappointingly, ground state of most primitive TMDs is non-magnetic. Then great efforts have been paid to explore how to introduce FM state into them. A variety of techniques are available to realize that objective, such as controlling the edge structure and saturation state, doping transition metal atoms, introducing defects or disorder mode, applying tensile strain and even by non-metal element adsorption.<sup>25,26,28–33</sup> For example, first-principle density functional theory simulation reveals that the presence of zigzag edge sites in MoS<sub>2</sub> leads to a strong spin polarization which locates on both edge S and Mo atoms, and that could cause a magnetic ground state at the grain boundaries.<sup>24,27,28</sup> Similar situations are proposed in zigzag edge WS<sub>2</sub> and GaS nanoribbons.<sup>26,34</sup> Introducing MoS<sub>2</sub>-triple vacancies in single-layer MoS<sub>2</sub> can also give rise to a net magnetic moment, while other defects

<sup>†</sup> Key Laboratory for Magnetism and Magnetic Materials of MOE, Lanzhou University, Lanzhou 730000, P. R. China. Fax: +86-0931-8914160; Tel: +86-0931-8912237; E-mail: gaodq@lzu.edu.cn; xueds@lzu.edu.cn

<sup>‡</sup> College of Electric and Information Engineering, Beifang University of Nationalities, Yinchuan 750021, P. R. China.

related to Mo and S atoms do not influence the non-magnetic ground state.<sup>35</sup> Mishra et al. investigated the long-range FM ordering in Mn-doped MoX<sub>2</sub> (X = S, Se, Te), WS<sub>2</sub> monolayers and attributed the origin for their FM ordering to exchange interactions between the localized Mn spins and the delocalized *p* spins of chalcogen atoms.<sup>29</sup> With edge effect, defects and doping in TMD materials, the non-magnetic and magnetic states are strongly dependent on which type of edge or defect is and where the positions of doping atoms are. Experimentally, since zigzag edge states and defects are generally present in few-layer TMDs, one would surmise that the ferromagnetism is widely exist in most few-layer TMD materials.<sup>34,36,37</sup> Besides, shape control during the crystal growth could benefit to the FM ordering because the TMD nanosheets with triangular and hexagonal shapes terminated by zigzag edges have been predicted to be magnetic.<sup>38,39</sup> Ion irradiation provides another effectively ways to introduce point defects as well as defect clusters in graphene and MoS<sub>2</sub> which could cause FM behavior among them.<sup>30,40</sup> Although these methods can be achieved experimentally, until now the effective manipulability associating with defects and edge states at nanoscale is still a challenge. Another alternative to manipulate magnetic behavior in TMDs is applying elastic strain. Recently, Shi et al. demonstrated that hydrogenated monolayer MoS<sub>2</sub> goes through a ground state transition from non-FM to FM under equibiaxial tensile strain, they attributed the emergence of spin polarization in MoS<sub>2</sub>-H to the strength of covalency weakened by applying tensile strain.<sup>33</sup>

Although theory calculations predict that FM ordering could be realized in variety of ingenious TMD nanostructures, the corresponding experimental results are rarely mentioned. Very weak FM has been observed in freestanding MoS<sub>2</sub> nanosheets and proton irradiated MoS<sub>2</sub> single crystal.<sup>30,41</sup> Meanwhile, thickish MoS<sub>2</sub> and WS<sub>2</sub> nanosheets could also show FM behavior.<sup>34,42</sup> However, to our knowledge, the strong FM in atomically thin MoS<sub>2</sub> and WS<sub>2</sub> is still lack of report; the reason may be the difficulties in synthesis few-layer MoS<sub>2</sub> and WS<sub>2</sub> because they tend to form zero-dimensional closed structures or one-dimensional nanotube during the experimental fabrications.<sup>43,44</sup> Recently, some reports suggested that chemical vapor deposition (CVD) is an useful method to grow high-quality, large-area and thin MoS<sub>2</sub> films.<sup>44-49</sup> Since the growth of MoS<sub>2</sub> is very sensitive to the substrate treatment and total pressure during the reaction, a complicated treatment prior to the growth or costly high-vacuum system is needed.<sup>45,46</sup> In addition, the substrate treatment makes it difficult to analyze the origin of FM signals. This motivated us to give a simple and efficient CVD method to grow few-layer MoS<sub>2</sub> and/or WS<sub>2</sub> nanosheets under normal pressure without any substrate treatment. On the other hand, a stable FM ordering with high Curie temperature (*T*<sub>C</sub>) is favorable in real spintronic devices. Therefore, investigation of high temper-

ature magnetic properties in those systems is necessary. In this paper, we present a simple and efficient CVD method for the preparation of atomically thin MoS<sub>2</sub> and WS<sub>2</sub> nanosheets. The structure and magnetic properties of these nanosheets were carefully characterized. By measuring the magnetization of both samples, the observed magnetic signals can be decomposed into diamagnetic (DM), paramagnetic (PM) and FM contributions. The FM contributions possess rather high *T*<sub>C</sub>. Those results could promote further understanding of FM ordering in TMD materials and may guide their potential applications in spintronics field.

## 2 Experimental section

Transition metal disulfide, MS<sub>2</sub> (M = Mo, W), nanosheets are synthesized in a hot-wall CVD system (Fig. S1). Silicon wafers with 280 nm thick native silicon oxide (SiO<sub>2</sub>/Si) are used as substrates. Before experiment, the silicon substrates are cleaned by piranha solution and flush with plenty of deionized water. In a typical procedure, 0.8 g of sulfur powder (99.5 %, J&K Chemical) was placed in an Al<sub>2</sub>O<sub>3</sub> crucible at the upstream entry of the furnace. 0.2 g of tungsten hexachloride (WCl<sub>6</sub>; W source) powder (99 %, J&K Chemical) or molybdenum trioxide (MoO<sub>3</sub>; Mo source) powder (99.5 %, J&K Chemical) was placed at the center of the furnace, the substrate was faced down and placed on the top of the source. The reaction process was kept in a high purity argon atmosphere, the furnace was heated up at a rate of 15 °C/min to the setting temperature under an argon gas flow rate of 2.5 SCCM (standard cubic centimeters per minute). To ensure an appropriate evaporation rate of sulfur source, the temperature for sulfur source was kept about 300 °C during the reaction. After held at a setting temperature for 15 min, the furnace cooled down naturally to room temperature. The reaction temperature range in our experiment was chosen from 650 °C to 850 °C, and it was found that to acquire high-quality MS<sub>2</sub> (M = Mo, W) nanosheets, the growth temperature should be below 750 °C.

Morphologies of the MS<sub>2</sub> (M = Mo, W) nanosheets were obtained using a scanning electron microscope (SEM; Hitachi S-4800) equipped with energy dispersive spectrometer (EDS). The crystal structure was analyzed from their X-ray diffraction (XRD; XPert PRO PHILIPS with Cu K<sub>α</sub> radiation) patterns. Microstructures of the samples were characterized using a transmission electron microscope (TEM; Tecnai TMG2F30, FEI) and high-resolution TEM (HRTEM) equipped with selected-area electron diffraction (SAED) and energy dispersive X-ray spectrometer (EDX). Raman spectra and photoluminescence (PL) were obtained using a Jobin-Yvon LabRam HR80 spectrometer (Horiba Jobin Yvon, Inc.) with a 532 nm line of Torus 50 mW diode-pumped solid-state laser under backscattering geometry. Atomic force mi-

croscopy (AFM; Dimension 3100 with Nanoscope IIIa controller, Veeco) was used to confirm the layer number of the nanosheets by measuring the thicknesses in tapping mode in air. The chemical bonding state and compositions of the samples were determined by X-ray photoelectron spectroscopy (XPS; VG Scientific ESCALAB-210 spectrometer) with monochromatic Mg  $K_{\alpha}$  X-rays source (1253.6 eV). Measurements of magnetic properties were performed using a Quantum Design MPMS magnetometer based on a superconducting quantum interference device (SQUID; Quantum Design, Inc.) and vibrating sample magnetometer equipped with high temperature chamber (VSM; VSM Model EV9, MicroSense, LLC). Thermogravimetric and differential thermal analysis (TG-DTA; Pyris Diamond TG/DTA analyzer, Perkin-Elmer Instrument) was employed to obtain the decomposition details of the  $\text{MoO}_3$  and  $\text{WCl}_6$  precursors, and to have accurate mass of the products (Fig. S7).

### 3 Results and discussion

The  $\text{MS}_2$  ( $M = \text{Mo}, \text{W}$ ) few-layer nanosheets were grown using vaporizable  $\text{WCl}_6$  or  $\text{MoO}_3$  as the cation source and sulfur as the anion source. The precursor materials react above boiling temperature to produce  $\text{MoS}_2$  or  $\text{WS}_2$  species and subsequently precipitate onto the substrate. TG-DTA analysis was carried out to hold the decomposition details of the precursors. With  $\text{MoO}_3$ , for example, the evaporation temperature is about 750 °C. So the reaction temperature range was selected from 650 °C to 850 °C every 50 °C. The  $\text{MoS}_2$  products grown at 700, 750, 800 and 850 °C are shown in Fig. 1(a) to (d), respectively. From the SEM images of 800 °C and 850 °C samples, it is confirmed that the Mo source,  $\text{MoO}_3$ , deposited on the substrate (deduced from the EDS results) due to the intense evaporation at such high temperature. After that, some  $\text{MoS}_2$  sheets grew out by sulphuring the  $\text{MoO}_3$  surface. By contrast, the samples grown at 700 °C and 750 °C have uniform profiles [Fig. 1(a) and (b)]. For 700 °C reaction temperature, we obtained triangular  $\text{MoS}_2$  nanosheets with a few micrometer edge length. This structure had been widely researched, and it is hard to measure the magnetic properties due to the very little mass of the product.<sup>39,46,48</sup> Therefore, in this paper, we focused on the samples grown at 750 °C which shows large-area, uniform and intensive morphology. Since the growth rate in 750 °C is faster than that of 700 °C condition, the nanosheets grow obviously out of the substrate and become freestanding. Notably, our growth mechanism is quite applicable for  $\text{WS}_2$  and may be easy to extend to other transition metal dichalcogenides systems.

Fig. 2(a)~(c) and (d)~(f) depict the SEM images of the  $\text{MoS}_2$  and  $\text{WS}_2$  nanosheets, and their corresponding EDS and XRD results. From the top view SEM images (a) and (d), it could clearly observe that  $\text{MoS}_2$  and  $\text{WS}_2$  grow into flower-

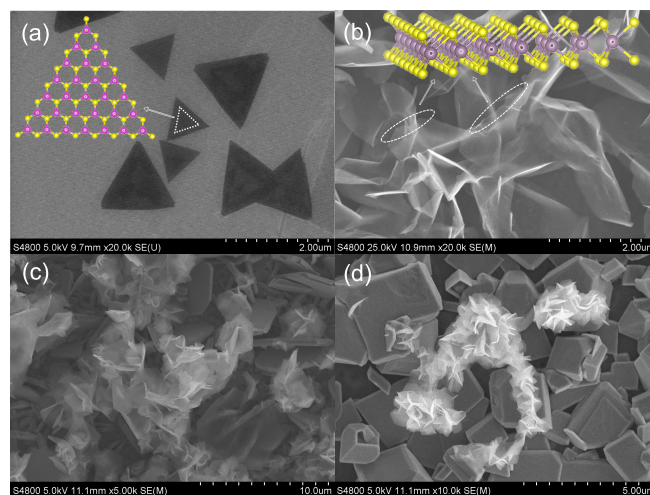


**Fig. 1**  $\text{MoS}_2$  nanosheets grow on  $\text{SiO}_2/\text{Si}$  substrates under different reaction temperatures. (a) Triangular  $\text{MoS}_2$  product with a few micrometer edge length is obtained at 700 °C. (b) Intensive and uniform  $\text{MoS}_2$  nanosheet grows at 750 °C. Insets show schematic illustrations of atomic-layered  $\text{MoS}_2$ . The pink and yellow atoms represent Mo and S, respectively.  $\text{MoS}_2$  sheets grow on  $\text{MoO}_3$  precursor which deposited on the substrate due to intense evaporation at (c) 800 °C and (d) 850 °C.

like nanosheets. The side view SEM images (b) and (e) also confirm that, and none of precursors has been found on the substrates due to the possible intense evaporation. EDS results for  $\text{MoS}_2$  and  $\text{WS}_2$  nanosheets reveal only Mo, S and W, S elements can be found in the samples. Si is from the  $\text{SiO}_2/\text{Si}$  substrate. Fig. 2(c) and (f) also display the XRD patterns of the nanosheet products. The reflection peaks can be assigned to the family lattice planes of hexagonal  $\text{MoS}_2$  (JCPDS card no.77-1716) and  $\text{WS}_2$  (JCPDS card no. 84-1398). Absence of any other peak suggests that there is no secondary phase present.

To further elucidate the crystal structure, TEM analysis was used to characterized the nanosheet samples. To do this, the nanosheets grown on silicon substrates were peeled off by ultrasound in alcohol. Since the nanosheet is easy to be separated from the substrate and becomes freestanding, we can transfer the sample to TEM grids by dropping the ultrasonic suspension on them. Fig. 3(a) and (d) show the HRTEM images for the  $\text{MoS}_2$  and  $\text{WS}_2$  nanosheets. From the inset of that, we found that the morphology of the samples are laminar. The HRTEM images clearly reveal the periodic atom arrangement of the  $\text{MoS}_2$  and  $\text{WS}_2$  nanosheets at selected locations. According to the periodic pattern in the lattice fringe image, the interplanar spacing was measured to be 0.27 nm and 0.28 nm, respectively, matching up with the (100) facet of  $\text{MoS}_2$  and  $\text{WS}_2$ . That the angle between [010] and [100] orientations is 120° reveals the hexagonal lattice structure of samples.

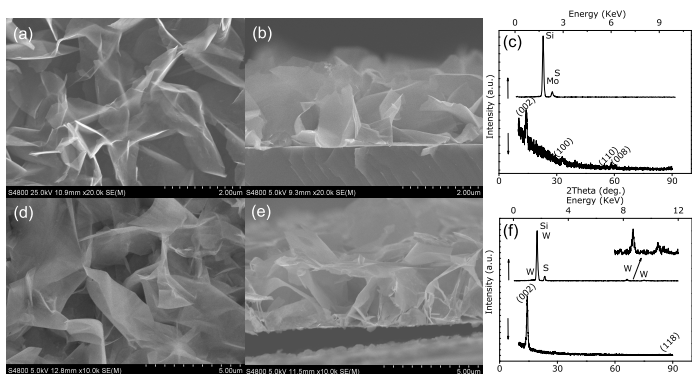


**Fig. 2** (a) Top view and (b) side view SEM images of the synthesized MoS<sub>2</sub> nanosheet grows on SiO<sub>2</sub>/Si substrate. (c) Relative XRD pattern of MoS<sub>2</sub> nanosheet. (d) Top view and (e) side view SEM images of the WS<sub>2</sub> nanosheet. (f) XRD result of WS<sub>2</sub> nanosheet.

Corresponding SAED results for the obtained MoS<sub>2</sub> and WS<sub>2</sub> nanosheets given in Fig. 3(b) and (e) reveal the single crystal samples in hexagonal structure. The crystal domain is at least one micrometre in lateral size because the SAED aperture size in our measurement is in micron dimension. The EDX results are also shown in Fig. 3(c) and (f). Only the elements Mo, S, Cu and C are presented in MoS<sub>2</sub> nanosheets; W, S, Cu, O and C are presented in WS<sub>2</sub> nanosheets. It can be understood that Cu and C are from the carbon membranes which hold the samples during measurement. O element may come from the adsorption O<sub>2</sub> by sample surface. Besides, no other impurity element has been detected.

In order to confirm the layer number of MoS<sub>2</sub> and WS<sub>2</sub> nanosheets, Raman and PL spectra were carried out. Generally, monolayer MoS<sub>2</sub> exhibits two strong bands at 384 and 400 cm<sup>-1</sup> which are associated with in-plane vibration E<sub>12g</sub> and out-of-plane vibration A<sub>1g</sub> modes, respectively.<sup>45–47</sup> As the layer number increased, the E<sub>12g</sub> and A<sub>1g</sub> bands move separated from each other. A redshift of about 2 cm<sup>-1</sup> for E<sub>12g</sub> band and a blueshift of about 5 cm<sup>-1</sup> for A<sub>1g</sub> band would be observed in the transition from monolayer MoS<sub>2</sub> to bulk. Those are similarly applied to WS<sub>2</sub> nanosheets, where the E<sub>12g</sub> band locates at 358 cm<sup>-1</sup> and the A<sub>1g</sub> at 418 cm<sup>-1</sup>.<sup>50,51</sup> In our case, as shown in red curve of Fig. 4(a) and (b), the E<sub>12g</sub> and A<sub>1g</sub> bands for the MoS<sub>2</sub> and WS<sub>2</sub> nanosheets are located at 382.6 cm<sup>-1</sup> and 404.8 cm<sup>-1</sup>; 355.2 cm<sup>-1</sup> and 419.0 cm<sup>-1</sup>, respectively. Note that the peak frequency difference between A<sub>1g</sub> and E<sub>12g</sub> modes ( $\Delta$ ) can be used to identify the number of layers in MoS<sub>2</sub> and WS<sub>2</sub>. The Raman spectra of bulk MoS<sub>2</sub> and WS<sub>2</sub> materials are also given in Fig. 4(a) and (b) (black curves) as reference. It can be seen that the  $\Delta$  value obtained from two nanosheet samples is about 22.2 cm<sup>-1</sup> and 63.8 cm<sup>-1</sup> which deviate from the bulk value of 26.8 cm<sup>-1</sup> and 65.2

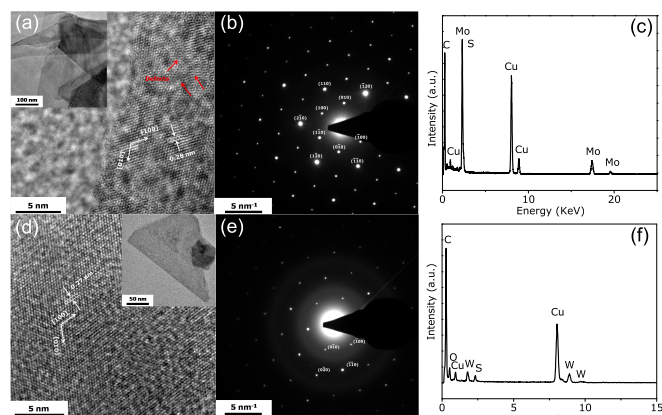


**Fig. 3** (a) High resolution TEM image of MoS<sub>2</sub> nanosheet. Inset shows TEM image where the HRTEM image is obtained. (b) Corresponding SAED pattern of MoS<sub>2</sub> nanosheet. (c) EDX spectrum of MoS<sub>2</sub> nanosheet. (d) HRTEM image of WS<sub>2</sub> nanosheet, the interplanar spacing of (100) is 0.27 nm. Inset shows the low-magnification TEM image of WS<sub>2</sub>. (e) SAED pattern of WS<sub>2</sub> nanosheet which shows a hexagonal structure. (f) Corresponding EDX result of WS<sub>2</sub> nanosheet.

cm<sup>-1</sup> markedly. Those  $\Delta$  value results indicate the existence of 1~2 layers in obtained MoS<sub>2</sub> nanosheet and 3~4 layers for WS<sub>2</sub> nanosheet.<sup>45,46,50</sup> In Fig. 4(c), the PL spectra show two pronounced emission peaks at 627 nm and 676 nm for MoS<sub>2</sub>, 616 nm and 633 nm for WS<sub>2</sub> sample. These emissions are attributed to the A1 and B1 direct excitonic transitions which are absent in the indirect bandgap bulk materials.<sup>50–52</sup> Because of the bandgap transform from direct to indirect one with the increased layer number, the PL emission intensity decreases obviously and can only be observed in few-layer nanosheet. The above PL spectra results also qualitatively demonstrate that our obtained MoS<sub>2</sub> and WS<sub>2</sub> samples are few-layer sheets. In Fig. 4(d) and (e), surface profile at the edge of MoS<sub>2</sub> sheets is given by tapping mode AFM measurement. The nanosheet was peeled off by ultrasound from the grown substrate and dropped to a silicon wafer for further tests. The sample shows a smooth and continuous surface with a roughness less than 0.2 nm. A clear and uniform edge is also observed. A typical AFM height profile at the edge of the nanosheet is shown in Fig. 4(f). The height profile extracts from the dash line which indicates in Fig. 4(e). The thickness of the observed MoS<sub>2</sub> layer is 1.31 nm which matches a bilayer MoS<sub>2</sub> sheet thickness and that further confirms the Raman results mentioned above.

In order to characterize the bonding state and composition of MoS<sub>2</sub> and WS<sub>2</sub> nanosheets, XPS measurements were taken on. Representative spectra of MoS<sub>2</sub> nanosheet and WS<sub>2</sub> nanosheet are shown in Fig. 5(a). The full XPS scanning from 0 to 1200 eV indicating only the elements Mo, S, C, O; and W,

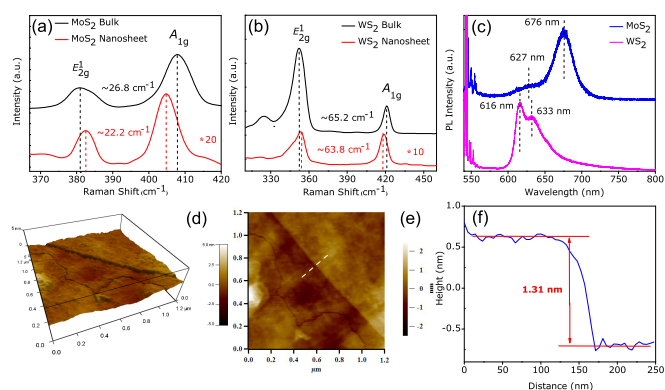


**Fig. 4** Raman spectra of (a) MoS<sub>2</sub> and (b) WS<sub>2</sub> nanosheets (red curves), bulk MoS<sub>2</sub> and WS<sub>2</sub> results are also shown in (a) and (b) as references (black curves), respectively. (c) PL of the synthesized MoS<sub>2</sub> and WS<sub>2</sub> nanosheets. Both Raman and PL measurement used a 532 nm excitation laser. (d) and (e) AFM images of a MoS<sub>2</sub> nanosheet. The synthesized nanosheet was peeled off by ultrasound from the grown substrate and dropped to a silicon wafer for the measurement. (f) AFM height profile for the MoS<sub>2</sub> nanosheet. The profile curve is extracted from the dash line shown in (e).

S, C, O are present in MoS<sub>2</sub> and WS<sub>2</sub> samples, respectively. The standard C 1s peak at 284.6 eV was used as a reference to correct the peak shifts and O is from O<sub>2</sub> adsorbed on the sample surface. More importantly, absence of any photoelectron peak in the range of 700 eV to 870 eV (Fig. S2) where Fe, Co and Ni 2p peaks are located suggests that magnetic impurities can be eliminated in our samples. This conclusion is also consistent with previous EDX results. Fig. 5(b) and (d) show the W 4f and Mo 3d core-level spectrum. The obvious spin-orbit splitting of the W 4f and Mo 3d is observed. Using a convolution of Lorentzian-Gaussian function under a Shirley background, the spectra can be well fitted. The peaks at 33.4 eV and 35.5 eV in Fig. 5(b) are identified as W 4f<sub>7/2</sub> and W 4f<sub>5/2</sub> in WS<sub>2</sub>. Another weak peak located at 39.1 eV is attributed to W 5p<sub>3/2</sub>.<sup>49,53</sup> The spectrum of Mo 3d consists of Mo 3d<sub>3/2</sub> at 229.9 eV and Mo 3d<sub>1/2</sub> at 233.0 eV which is coincident with Mo<sup>4+</sup> in MoS<sub>2</sub>. Another peak separated by 2.8 eV (227.1 eV) at lower binding energy corresponding to the S 2s peak of MoS<sub>2</sub>.<sup>44-46</sup> Above analysis also applies to S 2p core-level spectra. As shown in Fig. 5(c) and (e), two peaks located at 163.0 eV (162.8 eV) and 164.1 eV (163.9 eV) are attributed to S 2p<sub>3/2</sub> and S 2p<sub>1/2</sub> in WS<sub>2</sub> (MoS<sub>2</sub>). From the component detection results above, it can be concluded that the observed FM signals in WS<sub>2</sub> and MoS<sub>2</sub> nanosheets are intrinsic.

Through above characterization, we obtained high-quality few-layer MoS<sub>2</sub> and WS<sub>2</sub> nanosheets via a propagable CVD method. Then the effect of dimensionality to the magnetic property was studied on the nanosheets. Before experiment, the substrates were carefully cleaned. During the whole proce-

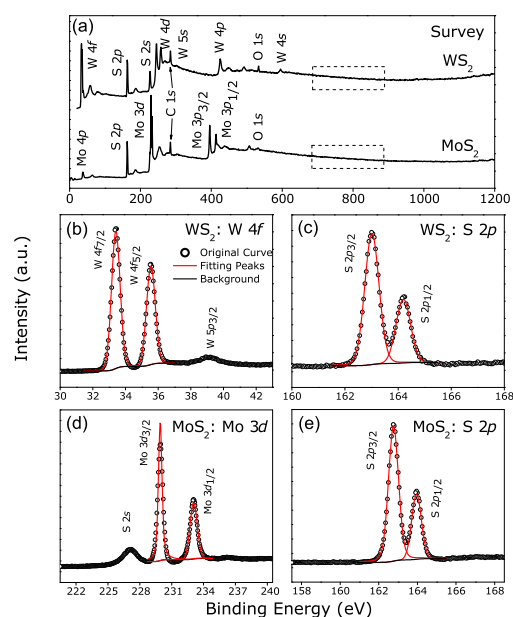


**Fig. 5** (a) XPS survey spectrum of MoS<sub>2</sub> and WS<sub>2</sub> nanosheets. Absence of magnetic elements Fe, Co and Ni has been confirmed (black dash line). High resolution scan and fitting results of (b) W 4f and (c) S 2p of WS<sub>2</sub> nanosheet; (d) Mo 3d and (e) S 2p of MoS<sub>2</sub> nanosheet.

cedure (cutting, reaction and measurement), special attentions, such as using plastic tweezers and spoons, were paid to avoid FM contamination. Moreover, we measured the magnetization versus applied field ( $M-H$ ) curves for the precursors (MoO<sub>3</sub>, WCl<sub>6</sub> and S) and silicon substrates (Fig. S3) which show the DM signals only. Fig. 6(a) depicts the  $M-H$  curves for the MoS<sub>2</sub> nanosheet performed at different temperatures where the DM signals have been deducted (the raw  $M-H$  curves are shown in Fig. S6). The curves measured above 300 K were carried out on a VSM, while others using the SQUID. As can be seen, the few-layer MoS<sub>2</sub> nanosheet shows clear FM hysteresis loops: the hysteresis behavior persists above 623 K; the saturation magnetization ( $M_s$ ) decreases from 1.08 emu/g at 10 K to 0.55 emu/g at 623 K, and the FM signal even vanishes at 973 K revealing that the  $T_C$  of the nanosheet is lower than that. The inset shows that the coercivity ( $H_c$ ) changes in different temperatures which is extracted from the hysteresis loops. The  $H_c$  drops with increasing temperatures from 241.3 Oe at 10 K to 48.3 Oe at 623 K. These features indicate a typical FM behavior of the MoS<sub>2</sub> nanosheet.<sup>30,54</sup> The hysteresis loops of WS<sub>2</sub> nanosheet measured at different temperatures are shown in Fig. 6(b). One can observe similar features with that of MoS<sub>2</sub> nanosheet: (I) distinct FM hysteresis behavior persists above 773 K; (II) the  $M_s$  decreases monotonously with the increased temperature; (III) there is gradual decrease of the  $H_c$  before  $T_C$ . Now we have observed hysteresis behaviors in

both few-layer MoS<sub>2</sub> and WS<sub>2</sub> nanosheets, further details of the FM ordering have been characterised by the zero-field-cooled (ZFC) and field-cooled (FC) measurements. ZFC-FC curves of the atomically thin MoS<sub>2</sub> and WS<sub>2</sub> films are given out in Fig. 6(c) and (d), respectively. The measurements were performed in the temperature range of 2 to 300 K at 500 Oe. The ZFC-FC curves for both samples indicate that there is only a single FM phase present. Neither superparamagnetic phase transition nor a progressive freezing of spins in spin-glass system has been found in ZFC curves, indicating that the observed FM signal is an intrinsic attribute rather than caused by FM impurities.<sup>55–57</sup> Since the applied field, in our case, is large than  $H_c$ , the ZFC curves would take close to the FC curves, but do not overlap below the  $T_C$ .<sup>54,58</sup> For both nanosheet samples shown in Fig. 6(c) and (d), it can be understood that the  $T_C$  of the FM phase is well above 300 K which has also been confirmed by the hysteresis loop results mentioned before.

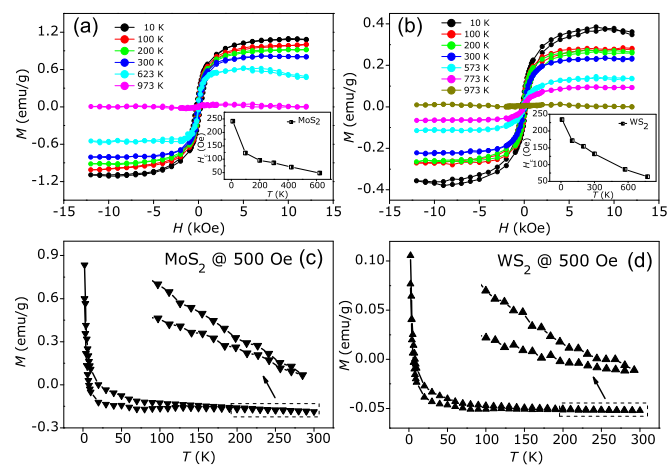


**Fig. 6**  $M$ - $H$  curves of (a) MoS<sub>2</sub> and (b) WS<sub>2</sub> nanosheets measured at different temperatures from 10 K to 973 K, the linear (PM + DM) signals have been subtracted. Dependence of coercivity  $H_c$  versus temperature  $T$  of the samples are shown in insets. ZFC-FC curves of MoS<sub>2</sub> and WS<sub>2</sub> nanosheets measured at 500 Oe are shown in (c) and (d).

The temperature-dependent magnetization ( $M$ - $T$ ) curves for both MoS<sub>2</sub> and WS<sub>2</sub> nanosheets were measured in the temperature range from 373 K to 973 K at 12 kOe and the results are shown in Fig. 7(a) and (c). For both curves, the large contribution represents the DM background, which is temperature independent. Besides, the magnetization declines gradually with the increasing temperature in a similar inverse relationship at the beginning, then an inflection point appears at about 850 K for MoS<sub>2</sub> nanosheet (slightly less than 850 K for WS<sub>2</sub> nanosheet). These can be explained by the presence of PM mixed with a FM phase. In order to separate the FM signal from the total magnetization (PM + DM + FM signals), we

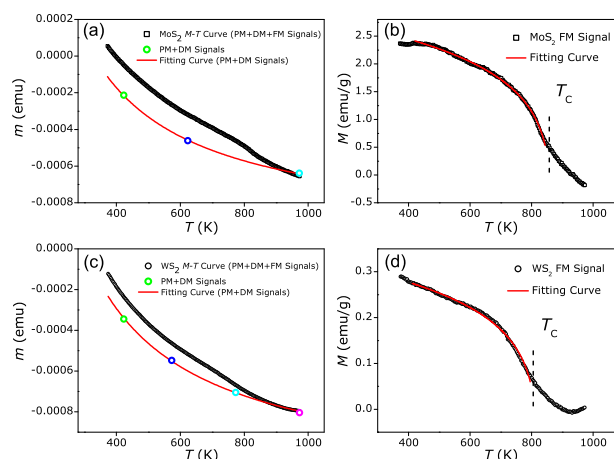


**Fig. 7**  $M$ - $T$  curves of (a) MoS<sub>2</sub> and (c) WS<sub>2</sub> nanosheets. Colour circles in the figure represent PM + DM magnetizations obtained by fitting the  $M$ - $H$  curve measured at that temperature. The red lines are the PM + DM magnetization fitting results with Eq. (1). The FM signals of MoS<sub>2</sub> and WS<sub>2</sub> nanosheets and fitting results with Eq. (2) are shown in (b) and (d).

firstly acquired the PM + DM magnetization by fitting the  $M$ - $H$  curves which measured at different temperatures in large field region [colour circles shown in Fig. 7(a) and (c)]. Then we fitted the temperature-dependent PM + DM magnetization ( $M_{p+d}$ ) by Curie's law:

$$M_{p+d}(T) = M_d + \frac{C}{T} \quad (1)$$

where  $M_d$  is the DM background,  $C$  is a constant related to the applied field and Curie constant,  $T$  is the temperature. The fitted curves of temperature-dependent PM + DM signals for MoS<sub>2</sub> and WS<sub>2</sub> nanosheets have been plotted in Fig. 7(a) and (c) (red curves), respectively. After that, the FM signals of our samples can be extracted by subtracting the PM + DM signals from the total magnetization, as shown in Fig. 7(b) and (d). The FM part can be well fitted by the following equation which is common for a FM material<sup>59,60</sup>:

$$M(T) = A \left(1 - \frac{T}{T_C}\right)^\beta \quad (2)$$

where  $A$  is a coefficient related to the spontaneous magnetization,  $T_C$  is the ferromagnetic Curie temperature, and  $\beta$  is the critical exponent. The best fitting curves ( $T < T_C$ ) for both samples are shown by red curves in Fig. 7(b) and (d). Corresponding fitting results by Eq. (1) and Eq. (2) are listed in Tab. 1. From that we obtained  $T_C$  of 865.5 K for MoS<sub>2</sub> nanosheet and 820.1 K for WS<sub>2</sub> nanosheet. Such higher  $T_C$  in our samples reveals that the FM of MoS<sub>2</sub> and WS<sub>2</sub> nanosheets is intrinsic rather than caused by FM metal and/or metal sulfides contaminations. More importantly, the  $T_C$  of our semi-

conducting MoS<sub>2</sub> and WS<sub>2</sub> nanosheets is much higher than that of traditional magnetic semiconductors and dilute magnetic semiconductors such as EuO ( $T_C < 100$  K), CoS<sub>2</sub> ( $T_C = 121$  K), GaMnAs ( $T_C < 200$  K) and ZnO:Mn ( $T_C < 300$  K). The achievement of high  $T_C$  FM in direct bandgap few-layer MoS<sub>2</sub> and WS<sub>2</sub> nanosheets gives them promising applications in spintronic devices. In addition, the critical exponents  $\beta$  for MoS<sub>2</sub> and WS<sub>2</sub> samples is 0.1283 and 0.1086, respectively, which matches well with the theoretical prediction of 2-dimensional Ising model ( $\beta = 1/8$ ).<sup>59</sup> The heating process of the  $M$ - $T$  measurement was in argon atmosphere to avoid that our nanosheet samples become oxidized. To make sure that the decline of the magnetization is not caused by the variousness of the structure and morphology of samples at high temperature, the SEM images of the nanosheets after annealing at 1000 °C in argon atmosphere are shown in Fig. S4. As can be seen, the morphology of both samples is not sensitive to the heat treatment in argon, and this further confirms that the high  $T_C$  FM in atomically thin MoS<sub>2</sub> and WS<sub>2</sub> nanosheets is intrinsic.

**Table 1** Fitting results for MoS<sub>2</sub> and WS<sub>2</sub> samples using Eq. (1) and (2).

Samples	MoS <sub>2</sub>	WS <sub>2</sub>
$C/(\text{emu/K})$	$3.190 \times 10^{-1}$	$3.427 \times 10^{-1}$
$M_d/(\text{emu})$	$-9.686 \times 10^{-4}$	$-1.151 \times 10^{-3}$
$A/(\text{emu/g})$	6.344	0.8757
$T_C/(\text{K})$	865.5	820.1
$\beta$	0.1283	0.1086

As discussed above, the magnetization of atomically thin MS<sub>2</sub> (M = Mo, W) nanosheets can be decomposed into three contributions: paramagnetism, diamagnetism and ferromagnetism. The  $T_C$  of those two systems can reach about 865 K and 820 K, respectively. In view of the mechanism for the formation of FM ordering in layered structure materials, such as graphene, *h*-BN and GaS, the defect-mediated mechanism as well as zigzag edge states are proposed to be the most general ones.<sup>26,37,61,62</sup> Large scale of extended defects and dislocations in *h*-BN are considered to be responsible for the formation of clear FM signals.<sup>62</sup> The defects in as-prepared BN have been demonstrated to be the bulk nature and that may be the reason why the observed  $M_s$  is robust. In fact, as seen from HRTEM observations, the defects and dislocations also exist naturally in our nanosheet systems (Fig. S5). Calculation results imply that the creation of MoS<sub>2</sub> triple vacancy leads to a significant net moment of  $2 \mu_B$  in monolayer MoS<sub>2</sub> system.<sup>33</sup> In particular, the net moment of MoS<sub>2</sub> triple vacancy could compensate the magnetization of zigzag edge MoS<sub>2</sub> which results in a promotion of net moment in supercell. Those striking feature of defects in MoS<sub>2</sub> and WS<sub>2</sub> thus may serve as a

crucial role in introducing FM in our nanosheet systems.<sup>32,33</sup>

Presence of zigzag edge states is another clear cause of FM in these layered structure materials. Just as in graphene and GaS nanoribbons, zigzag edges could lead to splitting of the energy bands near the Fermi level which suggests that the zigzag edge has net magnetic moment.<sup>26,37</sup> Huo et al. calculated the magnetic moments of edge S and W atoms in zigzag WS<sub>2</sub> ribbons which are 0.19 and 0.13  $\mu_B$  respectively, while the net moment of the inner atoms is zero.<sup>35</sup> Similar results have been found with the zigzag edge MoS<sub>2</sub>.<sup>24,28</sup> In addition, through the research on the magnetic properties for zigzag edge graphene analogues of MoS<sub>2</sub>, WS<sub>2</sub> and *h*-BN with different numbers of layers, it is found that there is increase in the magnetic moment with the decreasing number of layers.<sup>37</sup> In our case, the thickness of MoS<sub>2</sub> nanosheet was demonstrated only 1~2 molecular layers, and slightly thicker for WS<sub>2</sub> nanosheet which shows 3~4 molecular layers. Such an ultrathin size of our samples may be the reason why the observed  $M_s$  is one to two orders larger than other defects or interface induced FM systems involving nanoparticles or thin films.<sup>63-65</sup> Therefore, it is speculated that the robust FM signals in MoS<sub>2</sub> and WS<sub>2</sub> nanosheet grown via the CVD method have two possible sources: (I) the defects and dislocations produced naturally during the growth process which can give rise to magnetic moment; (II) the presence of zigzag edge states that could cause the edge atoms has unpaired electrons and lead to the magnetic moment occurring at the edges. Besides, the  $T_C$  of FM signals in our nanosheet samples is much higher than that of conventional magnetic semiconductors, that brings advantages to the stability of spintronic devices based on TMD materials in potential application.

## 4 Conclusions

In summary, we have successfully synthesized atomically thin MoS<sub>2</sub> and WS<sub>2</sub> nanosheets on SiO<sub>2</sub>/Si substrates via the simple and efficient CVD method. Corresponding morphology and structure characterizations reveal that a flower-like and uniform profile is obtained in high crystallinity MoS<sub>2</sub> and WS<sub>2</sub> nanosheets with hexagonal lattice structure. Raman and AFM measurements indicate the MoS<sub>2</sub> nanosheet shows a monolayer to bilayer thickness, while 3~4 layer molecules are found in WS<sub>2</sub> nanosheet. PL spectra reveal that strong layer-dependent luminescence emerge in both samples. XPS measurements are used to ensure no any valence change or impurity element present in our samples. Magnetic measurements show a distinct FM behavior in both MoS<sub>2</sub> and WS<sub>2</sub> nanosheets. Three magnetic contributions (PM + DM + FM signals) can be identified by numerical fittings. Moreover, the FM signals exhibit  $T_C$  (865.5 K for MoS<sub>2</sub> and 820.1 K for WS<sub>2</sub>) that is well above room temperature. By comparing with the models and calculation results in literature, we attributed the magnetic

properties to the defects and dislocations produced during the growth process as well as the presence of zigzag edge states at the edge of the nanosheets. Our findings do not only give an insight into the magnetic properties of atomically thin MoS<sub>2</sub> and WS<sub>2</sub> nanosheets but also pave the way for the future applications owing to their high  $M_s$  and excellent temperature stability.

## ACKNOWLEDGEMENTS

This work is supported by National Basic Research Program of China (Grant No. 2012CB933101), the National Natural Science Foundation of China (Grant Nos. 51371093, 11034004 and 11474137), Program for Changjiang Scholars and Innovative Research Team in University (Grant No. IRT1251), and Specialized Research Fund for the Doctoral Program of Higher Education (Grant No. 20130211130003).

## References

- 1 B. Radisavljevic, A. Radenovic, J. Brivio, V. Giacometti and A. Kis, *Nat. Nanotechnol.*, 2011, **6**, 147–150.
- 2 S. Kim, A. Konar, W. Hwang, J. H. Lee, J. Lee, J. Yang, C. Jung, H. Kim, J. Yoo, J. Choi, Y. W. Jin, S. Y. Lee, D. Jena, W. Choi and K. Kim, *Nat. Commun.*, 2012, **3**, 1011.
- 3 J. S. Ross, S. Wu, H. Yu, N. J. Ghimire, A. M. Jones, G. Aivazian, J. Yan, D. G. Mandrus, D. Xiao, W. Yao and X. Xu, *Nat. Commun.*, 2013, **4**, 1474.
- 4 K. Mak, K. He, J. Shan and T. F. Heinz, *Nat. Nanotechnol.*, 2012, **7**, 494–498.
- 5 O. Lopez-Sanchez, D. Lembke, M. Kayci and A. Kis, *Nat. Nanotechnol.*, 2013, **8**, 497–501.
- 6 I. Popov, G. Seifert and D. Tomanek, *Phys. Rev. Lett.*, 2012, **108**, 156802.
- 7 Z. Yin, H. Li, H. Li, L. Jiang, Y. Shi, Y. Sun, G. Lu, Q. Zhang, X. Chen and H. Zhang, *ACS Nano*, 2012, **6**, 74.
- 8 T. Georgiou, R. Jalil, B. D. Belle, L. Britnell, R. V. Gorbachev, S. V. Morozov, Y. Kim, A. Gholinia, S. J. Haigh, O. Makarovsky, L. Eaves, L. A. Ponomarenko, A. K. Geim, K. S. Novoselov and A. Mishchenko, *Nat. Nanotechnol.*, 2013, **8**, 100–103.
- 9 S. Tongay, J. Zhou, C. Ataca, J. Liu, J. S. Kang, T. S. Matthews, L. You, J. Li, J. C. Grossman and J. Wu, *Nano Lett.*, 2013, **13**, 2831–2836.
- 10 K. F. Mak, C. Lee, J. Hone, J. Shan and T. F. Heinz, *Phys. Rev. Lett.*, 2010, **105**, 136805.
- 11 A. Kuc, N. Zibouche and T. Heine, *Phys. Rev. B*, 2011, **83**, 245213.
- 12 F. Schwierz, *Nat. Nanotechnol.*, 2011, **6**, 135–136.
- 13 G. L. Frey, S. Elani, M. Homyonfer, Y. Feldman and R. Tenne, *Phys. Rev. B*, 1998, **57**, 6666.
- 14 N. Huo, S. Yang, Z. Wei, S. Li, J. Xia and J. Li, *Sci. Rep.*, 2014, **4**, 5209.
- 15 S. Yang, Y. Li, X. Wang, N. Huo, J.-B. Xia, S.-S. Li and J. Li, *Nanoscale*, 2014, **6**, 2582–2587.
- 16 S. Yang, S. Tongay, Q. Yue, Y. Li, B. Li and F. Lu, *Sci. Rep.*, 2014, **4**, 5442.
- 17 J. Xiao, D. W. Choi, L. Cosimbescu, P. Koech, J. Liu and J. P. Lemmon, *Chem. Mater.*, 2010, **22**, 4522–4524.
- 18 M. Mosleh, N. D. Atnafu, J. H. Belk and O. M. Nobles, *Wear*, 2009, **267**, 1220.
- 19 J. Feng, L. L. Peng, C. Z. Wu, X. Sun, S. L. Hu, C. W. Lin, J. Dai, J. L. Yang and Y. Xie, *Adv. Mater.*, 2012, **24**, 1969.
- 20 H. H. Wu, R. Yang, B. M. Song, Q. S. Han, J. Y. Li, Y. Zhang, Y. Fang, R. Tenne and C. Wang, *ACS Nano*, 2011, **5**, 1276–1281.
- 21 H. Farag, A. N. A. El-Hendawy, K. Sakanishi, M. Kishida and I. Mochida, *Appl. Catal. B*, 2009, **91**, 189–197.
- 22 K. Chang, W. Chen, L. Ma, H. Li, H. Li, F. Huang, Z. Xu, Q. Zhang and J.-Y. Lee, *J. Mater. Chem.*, 2011, **21**, 6251–6257.
- 23 D. Voiry, H. Yamaguchi, J. Li, R. Silva, D. C. B. Alves, T. Fujita, M. Chen, T. Asefa, V. B. Shenoy, G. Eda and M. Chhowalla, *Nat. Mater.*, 2013, **12**, 850–855.
- 24 H. Pan and Y. W. Zhang, *J. Mater. Chem.*, 2012, **22**, 7280–7290.
- 25 Y. D. Ma, Y. Dai, M. Guo, C. W. Niu, Y. T. Zhu and B. B. Huang, *ACS Nano*, 2012, **6**, 1695.
- 26 Y. Zhou, S. Li, W. Zhou, X. Zu and F. Gao, *Sci. Rep.*, 2014, **4**, 5773.
- 27 R. Shidpour and M. Manteghian, *Nanoscale*, 2010, **2**, 1429–1435.
- 28 Y. Li, Z. Zhou, S. Zhang and Z. Chen, *J. Am. Chem. Soc.*, 2008, **130**, 16739–16744.
- 29 R. Mishra, W. Zhou, S. J. Pennycook, S. T. Pantelides and J.-C. Idrobo, *Phys. Rev. B*, 2013, **88**, 144409.
- 30 S. Mathew, K. Gopinadhan, T. K. Chan, X. J. Yu, D. Zhan, L. Cao, A. Rusydi, M. B. H. Breese, S. Dhar, Z. X. Shen, T. Venkatesan and J. T. L. Thong, *Appl. Phys. Lett.*, 2012, **101**, 102103.
- 31 S. W. Han, Y. H. Hwang, S.-H. Kim, W. S. Yun, J. D. Lee, M. G. Park, S. Ryu, J. S. Park, D.-H. Yoo, S.-P. Yoon, S. C. Hong, K. S. Kim and Y. S. Park, *Phys. Rev. Lett.*, 2013, **110**, 247201.
- 32 Y. Ma, Y. Dai, M. Guo, C. Niu, J. Lu and B. Huang, *Phys. Chem. Chem. Phys.*, 2011, **13**, 15546–15553.
- 33 H. Shi, H. Pan, Y.-W. Zhang and B. I. Yakobson, *Phys. Rev. B*, 2013, **88**, 205305.

- 34 N. Huo, Y. Li, J. Kang, R. Li, Q. Xia and J. Li, *Appl. Phys. Lett.*, 2014, **104**, 202406.
- 35 C. Ataca, H. Sahin, E. Akturk and S. Ciraci, *J. Phys. Chem. C*, 2011, **115**, 3934–3941.
- 36 S. Tongay, S. S. Varnoosfaderani, B. R. Appleton, J. Wu and A. F. Hebard, *Appl. Phys. Lett.*, 2012, **101**, 123105.
- 37 C. N. R. Rao, H. S. S. R. Matte, K. S. Subrahmanyam and U. Maitra, *Chem. Sci.*, 2012, **3**, 45–52.
- 38 S. Najmaei, Z. Liu, W. Zhou, X. Zou, G. Shi, S. Lei, B. I. Yakobson, J.-C. Idrobo, P. M. Ajayan and J. Lou, *Nat. Mater.*, 2013, **12**, 754–759.
- 39 H. Liu, M. Si, S. Najmaei, A. T. Neal, Y. Du, P. M. Ajayan, J. Lou and P. D. Ye, *Nano Lett.*, 2013, **13**, 2640–2646.
- 40 P. Esquinazi, D. Spemann, R. Hohne, A. Setzer, K. H. Han and T. Butz, *Phys. Rev. Lett.*, 2003, **91**, 227201.
- 41 D. Gao, M. Si, J. Li, J. Zhang, Z. Zhang, Z. Yang and D. Xue, *Nanoscale Res. Lett.*, 2013, **8**, 129.
- 42 J. Zhang, J. M. Soon, K. P. Loh, J. Yin, J. Ding, M. B. Sullivan and P. Wu, *Nano Lett.*, 2007, **7**, 2370–2376.
- 43 A. M. Seayad and D. M. Antonelli, *Adv. Mater.*, 2004, **16**, 765–777.
- 44 K. K. Liu, W. Zhang, Y. H. Lee, Y. C. Lin, M. T. Chang, C. Y. Su, C. S. Chang, H. Li, Y. Shi, H. Zhang, C. S. Lai and L. J. Li, *Nano Lett.*, 2012, **12**, 1538–1544.
- 45 Y. Yu, C. Li, Y. Liu, L. Su, Y. Zhang and L. Cao, *Sci. Rep.*, 2013, **3**, 1866.
- 46 Y.-H. Lee, X.-Q. Zhang, W. Zhang, M.-T. Chang, C.-T. Lin, K.-D. Chang, Y.-C. Yu, J. T.-W. Wang, C.-S. Chang, L.-J. Li and T.-W. Lin, *Adv. Mater.*, 2012, **24**, 2320–2325.
- 47 Y. Zhan, Z. Liu, S. Najmaei, P. M. Ajayan and J. Lou, *Small*, 2012, **8**, 966–971.
- 48 J. Xia, X. Huang, L.-Z. Liu, M. Wang, L. Wang, B. Huang, D.-D. Zhu, J.-J. Li, C.-Z. Gu and X.-M. Meng, *Nanoscale*, 2014, **6**, 8949–8955.
- 49 J.-K. Huang, J. Pu, C.-L. Hsu, M.-H. Chiu, Z.-Y. Juang, Y.-H. Chang, W.-H. Chang, Y. Iwasa, T. Takenobu and L.-J. Li, *ACS Nano*, 2014, **8**, 923–930.
- 50 W. Zhao, Z. Ghorannevis, K. K. Amara, J. R. Pang, M. Toh, X. Zhang, C. Kloc, P. H. Tan and G. Eda, *Nanoscale*, 2013, **5**, 9677–9683.
- 51 H. R. Gutiérrez, N. Perea-López, A. L. Elías, A. Berkdemir, B. Wang, R. Lv, F. López-Urías, V. H. Crespi, H. Terrones and M. Terrones, *Nano Lett.*, 2013, **13**, 3447–3454.
- 52 A. Splendiani, L. Sun, Y. Zhang, T. Li, J. Kim, C.-Y. Chim, G. Galli and F. Wang, *Nano Lett.*, 2010, **10**, 1271–1275.
- 53 S. B. Sadale, S. R. Barman and P. S. Patil, *Appl. Surf. Sci.*, 2007, **253**, 3489–3495.
- 54 Y. Wang, L. Li, S. Prucnal, X. Chen, W. Tong, Z. Yang, F. Munnik, K. Potzger, W. Skorupa, S. Gemming, M. Helm and S. Zhou, *Phys. Rev. B*, 2014, **89**, 014417.
- 55 J. B. Yi, J. Ding, Y. P. Feng, G. W. Peng, G. M. Chow, Y. Kawazoe, B. H. Liu, J. H. Yin and S. Thongmee, *Phys. Rev. B*, 2007, **76**, 224402.
- 56 M. Ghosh, K. Biswas, A. Sundaresan and C. N. R. Rao, *J. Mater. Chem.*, 2006, **16**, 106–111.
- 57 S. D. Tiwari and K. P. Rajeev, *Phys. Rev. B*, 2005, **72**, 104433.
- 58 M. Jamet, A. Barski, T. Devillers, V. Poydenot, R. Du Jardin, P. Bayle-Guillemaud, J. Rothman, E. Bellet-Amalric, A. Marty, J. Cibert, R. Mattana and S. Tatarenko, *Nat. Mater.*, 2006, **5**, 653.
- 59 H. E. Stanley, *Introduction to Phase Transitions and Critical Phenomena*, Oxford University Press, Oxford, 1987.
- 60 T. T. Carvalho, J. R. A. Fernandes, J. P. de la Cruz, J. V. Vidal, N. A. Sobolev, F. Figueiras, S. Das, V. S. Amaral, A. Almeida, J. A. Moreira and P. B. Tavares, *J. Alloys Comp.*, 2013, **554**, 97–103.
- 61 Z. Zhang, X. C. Zeng and W. Guo, *J. Am. Chem. Soc.*, 2011, **133**, 14831–14838.
- 62 B. Song, J. C. Han, J. K. Jian, H. Li, Y. C. Wang, H. Q. Bao, W. Y. Wang, H. B. Zuo, X. H. Zhang, S. H. Meng and X. L. Chen, *Phys. Rev. B*, 2009, **80**, 153203.
- 63 A. Sundaresan and C. N. R. Rao, *Nano Today*, 2009, **4**, 96–106.
- 64 D. Gao, Z. Zhang, Z. Yang and D. Xue, *Appl. Phys. Lett.*, 2012, **101**, 132416.
- 65 T. S. Heng, D.-C. Qi, T. Berlijn, J. B. Yi, K. S. Yang, Y. Dai, Y. P. Feng, I. Santoso, C. Sánchez-Hanke, X. Y. Gao, A. T. S. Wee, W. Ku, J. Ding and A. Rusydi, *Phys. Rev. Lett.*, 2010, **105**, 207201.